

Polarization of Nonlinear Thomson Scattering from a High-Intensity Laser Focus

Brittni Tasha Pratt

A thesis submitted to the faculty of
Brigham Young University
in partial fulfillment of the requirements for the degree of
Master of Science

Michael Ware, Chair
Justin Peatross
Karine Chesnel

Department of Physics and Astronomy
Brigham Young University

Copyright © 2020 Brittni Tasha Pratt

All Rights Reserved

ABSTRACT

Polarization of Nonlinear Thomson Scattering from a High-Intensity Laser Focus

Brittini Tasha Pratt
Department of Physics and Astronomy, BYU
Master of Science

Thomson scattering from free electrons in a high-intensity laser focus has been widely studied analytically, but not many measurements of this scattering have been made. We measure polarization-resolved nonlinear Thomson scattering from electrons in a high-intensity laser focus using a parabolic mirror. The weak scattering signal is distinguished from background noise using single-photon detectors and nanosecond time-resolution to distinguish a prompt scattering signal from noise photons. The azimuthal and longitudinal components of the fundamental, second, and third harmonics were measured. Our measurements reasonably match theoretical results, but also show some asymmetry in the emission patterns.

Keywords: Nonlinear Thomson scattering, free electrons, high-intensity, polarization, photon detector, parabolic mirror

ACKNOWLEDGMENTS

I am so grateful for Dr. Ware and Dr. Peatross who gave me the opportunity to participate in this research project. I have learned so much from them and am so thankful for their guidance. I also would like to express appreciation for my husband, Chris, and our daughters, Madison and Paisley. Their love and support have made it possible for me to continue my education.

Contents

Table of Contents	iv
List of Figures	v
1 Introduction and Background	1
1.1 Thomson Scattering	1
1.2 Nonlinear Thomson Scattering	3
1.3 Previous Research on Nonlinear Thomson Scattering	4
1.4 Quantum vs. Classical Electron	7
1.5 Overview	10
2 Theoretical and Computational Model	12
2.1 Equations of Motion for an Electron in a High Intensity Laser Field	12
2.2 Radiation from Free Electrons	16
3 Methods	21
3.1 Experimental Setup	21
3.2 Positioning the Detector	23
3.3 Photon Counting	24
4 Results	27
4.1 Measurements of Nonlinear Thomson Scattering	27
4.1.1 Fundamental Radiation	27
4.1.2 Second Harmonic	28
4.1.3 Third Harmonic	29
4.2 Summary	30
4.3 Future Work	30
Bibliography	31
Index	33

List of Figures

1.1	Electromagnetic Dipole Radiation	2
1.2	Electron in an Electromagnetic Field	3
1.3	Harmonic Orders Observed by Yu et al.	5
1.4	Third Harmonic Observed by the Umstadter Group	6
1.5	Second Harmonic Observed by Babzien	7
1.6	Intensity Area for Helium Ionization	8
1.7	Experimental Setup for Previous Research	9
1.8	Measured Photon Counts as a Function of Prepulse Delay and Laser Intensity	9
2.1	Orbit of Electron in High Intensity Beam	13
2.2	Electron Trajectory in High Intensity Beam	14
2.3	Trajectories of Ten Electrons in a High Intensity Beam	15
2.4	Nonlinear Thomson Scattering	19
2.5	Far-field Radiation Patterns as a Function of Angle	20
3.1	Experimental Setup	22
3.2	Total Number of Photons as a Function of Arrival Time	25
4.1	Fundamental Radiation Results	28
4.2	Second Harmonic Radiation Results	28

4.3 Third Harmonic Radiation Results 29

Chapter 1

Introduction and Background

1.1 Thomson Scattering

In the early 1900's, scientist J. J. Thomson described the radiation emitted when unbound charged particles scatter electromagnetic radiation. This radiation, now known as Thomson scattering, can be well-described by classical electromagnetic theory. Thomson scattering is an elastic scattering process, meaning that the kinetic energy of the charged particle and the frequency of the scattered light are conserved. It is the low-energy limit of Compton scattering [1].

The motion of a charged particle in an electromagnetic wave is described by the Lorentz force:

$$\frac{d\mathbf{p}}{dt} = q(\mathbf{E} + \mathbf{u} \times \mathbf{B}), \quad (1.1)$$

where q is the charge of the particle, \mathbf{E} is the electric field, \mathbf{B} is the magnetic field, and \mathbf{p} is the momentum given by

$$\mathbf{p} = \gamma m \mathbf{u}, \quad (1.2)$$

where

$$\gamma = \frac{1}{\sqrt{1 - u^2/c^2}}. \quad (1.3)$$

When the particle experiences a low intensity oscillating electromagnetic field, the motion of the particle is nonrelativistic, meaning that $u \ll c$. This makes it so the $\mathbf{u} \times \mathbf{B}$ term in the Lorentz force law is negligible and the magnetic force has little impact on the trajectory of the particle. In this case, Eq. (1.1) simplifies to $\frac{d\mathbf{p}}{dt} = q\mathbf{E}$. The Lorentz factor γ in the momentum approaches one in the non-relativistic case, so that $\mathbf{p} = m\mathbf{u}$.

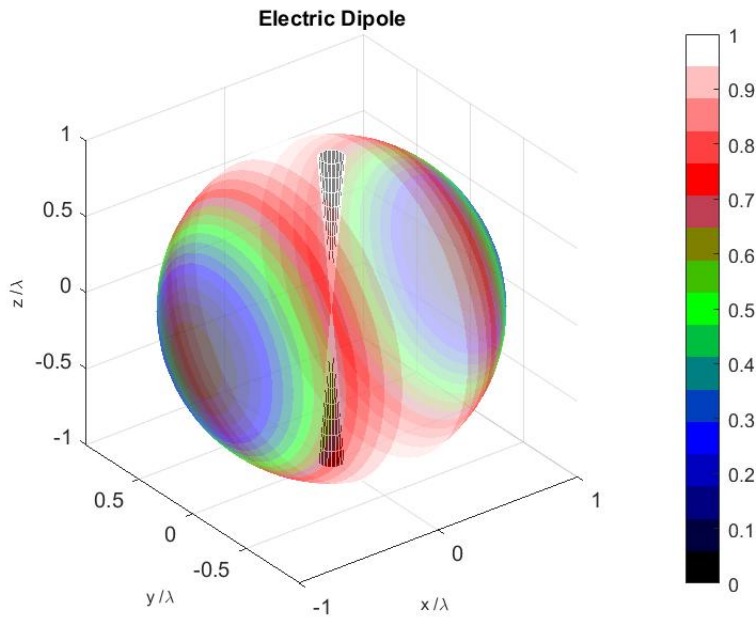


Figure 1.1 Radiation from an oscillating electron located at the center of the sphere. The laser focus is represented by the black cones and the color scale represents different values of intensity where white is the highest intensity and black is the lowest intensity.

In this low-intensity regime, the particle accelerates in the same direction as the electric field and radiates as an electric dipole. Figure 1.1 shows the radiation pattern from such a dipole, where an oscillating electron is located at the center of the sphere. A laser linearly polarized in the x -direction is represented by the black cones. The radiation from the particle carries the same frequency as that of the driving electromagnetic wave.

1.2 Nonlinear Thomson Scattering

In the previous section, we discussed a particle in a low intensity oscillating electromagnetic field which allowed us to ignore the magnetic field component when determining the motion of the particle. Now we will consider a particle in a high-intensity electromagnetic field.

The motion of a particle at high-intensity is relativistic, so γ in the momentum becomes appreciably larger than one and $\mathbf{u} \times \mathbf{B}$ in Eq. (1.1) can no longer be neglected. The motion of the particle is now significantly influenced by the magnetic field as well as the electric field. Figure 1.2 shows the patterns that an electron traces in (a) a low intensity field versus (b) a high-intensity field in the average rest frame of the electron. In this figure, the electric field oscillates in the x -direction and the magnetic field in the z -direction. In Fig. 1.2a, we see the pattern traced by an electron moving nonrelativistically and that the electron simply oscillates in the direction of the electric field. Figure 1.2b displays the figure-eight pattern traced by an electron moving relativistically since it is also influenced by the magnetic field component. From the lab frame, the figure-eight pattern is not apparent. The trajectory of the electron from the lab frame will be discussed in greater detail in Chapter 2.

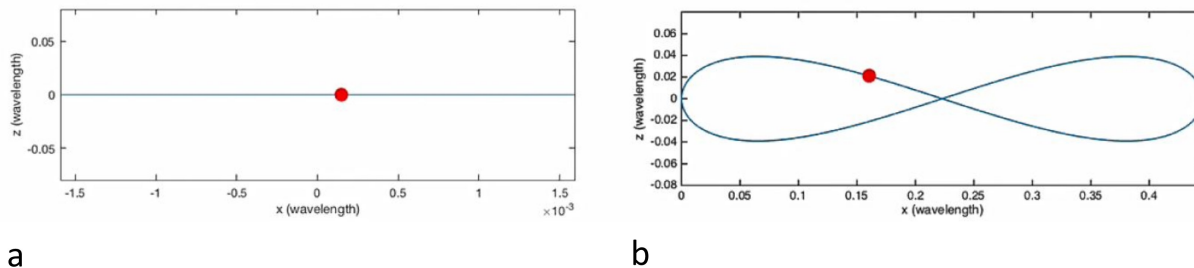


Figure 1.2 Motion of an electron in a low intensity field ($2 \times 10^{16} \text{ W/cm}^2$) (a) and a high-intensity ($2 \times 10^{19} \text{ W/cm}^2$) field (b) in the average rest frame of the electron.

As the particle in a high-intensity field oscillates nonlinearly, it radiates photons at harmonic frequencies of the incident light [2]. This is known as nonlinear Thomson scattering. We will review

the equations that describe the motion and radiation of a particle in a high-intensity field in greater detail in Chapter 2.

1.3 Previous Research on Nonlinear Thomson Scattering

Many analytical studies have been done on nonlinear Thomson scattering [3–5]. A topic of interest has been the potential of using nonlinear Thomson scattering from electrons in intense laser pulses to generate short-pulse x rays. These x rays could be used in many applications, such as medical imaging and x-ray spectroscopy [1, 3, 6]. In 1993, Eric Esarey et al. investigated the possibility of using a laser synchrotron source based on nonlinear Thomas scattering to produce high energy ultrashort x-ray pulses. His model showed that this may be a viable method for producing these x rays, as a laser synchrotron source has many attractive features such as compactness and low cost [3].

The harmonic orders of nonlinear Thomson scattering from free electrons have also been studied by many researchers, most notably by Sarachik and Schappert in 1970. Their theoretical analysis included the solutions for the electron trajectory, radiated power, momentum, and harmonics in the laboratory frame and the average rest frame of the electron [4]. We will review the equations of motion for the electron in the average rest frame in greater detail in Chapter 2.

In 1998, Wei Yu et al. also investigated the harmonic orders of nonlinear Thomson scattering analytically. Their study was based on nonlinear Thomson scattering from counterstreaming relativistic electrons in an ultraintense laser beam. In their study, they considered a high-intensity flat-top laser of circular polarization with an electron orbiting in the plane perpendicular to the laser propagation. Figure 1.3a shows the angular distribution of scattered radiation for the 1st to the 50th harmonics in the average rest frame of the electron. The scattered radiation for the fundamental frequency peaks in the plane normal to the electron orbit, whereas the radiation for the higher

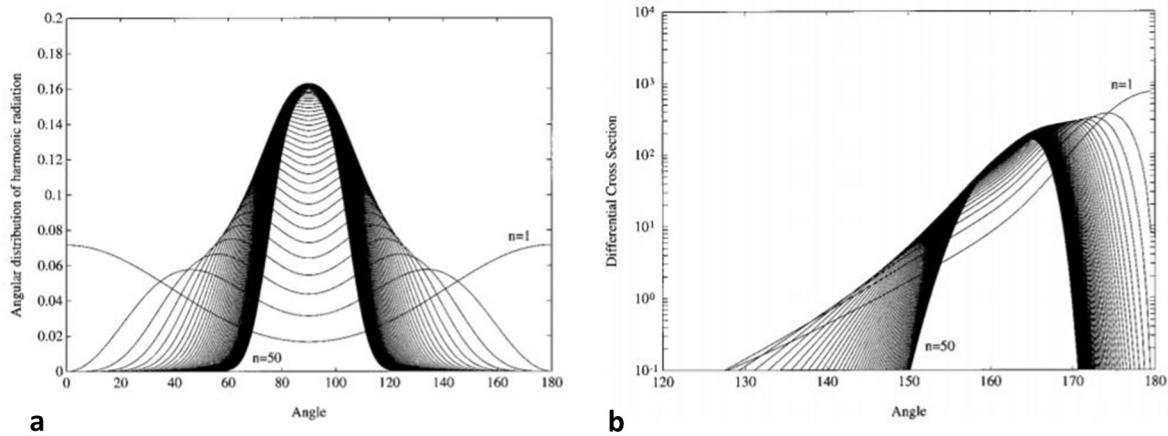


Figure 1.3 (a) Angular distribution of the 1st to the 50th harmonics in the average rest frame of the electron (b) Differential cross section of the scattered radiation for the 1st to the 50th harmonics in the laboratory frame. The peak in the higher harmonics peak in the plane containing the electron orbit from the average rest frame of the electron and shifts to around 162° from the lab frame. Figure taken from [5].

harmonics peak in the plane that contains the electron orbit. Figure 1.3b shows the differential cross section of the scattered radiation with respect to angle in the laboratory frame. The fundamental radiation peaks in the opposite direction to that of the incident laser, and the higher harmonics, which peak in the plane that contains the electron orbit in the average rest frame of the electron, shift forward to an angle of about 162° in the laboratory frame [5]. Their results show that relativistic electrons in an ultraintense laser beam scatter radiation mainly in the higher harmonics and that the Doppler effect causes a frequency up-shift. Using the effects of high harmonic generation and Doppler shift, the radiation scattered can be of very short wavelength and thus strong frequency up-conversion is possible [5].

The first measurements of nonlinear Thomson scattering were done by the Umstadter group in 1998 [2]. They measured nonlinear Thomson scattering from free electrons using a high-intensity pulse laser system focused onto a helium gas jet. Their results show the second and third harmonics radiated from the electrons. Figure 1.4 shows the radiation as a function of azimuthal angle for the third harmonic; the solid line represents the theoretical prediction, and the black dots represent their

measured results. These were groundbreaking results since nonlinear Thomson scattering had never been measured before, and their study confirmed the analytical models theorized by researchers.

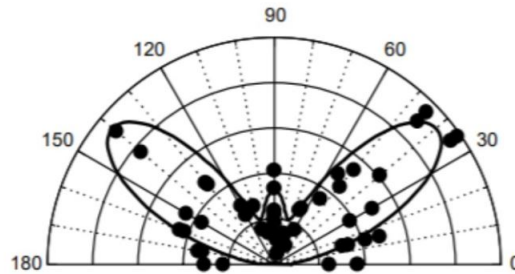


Figure 1.4 Third harmonic from the Thomson scattering in plasma for 0.8 J pulse energy and $6.2 \times 10^{19} \text{ cm}^{-3}$ electron density at $\theta = 90^\circ$ is shown with respect to angle detected. The theoretical prediction is shown with the black line and the experimental measurements is shown with the black dots. Figure taken from [2].

In 2006, the second harmonic of nonlinear Thomson scattering was also measured by Marcus Babzien et al. In their experiment, they collided laser pulses with electron beams and found the angular distribution of the intensity for the second harmonic of nonlinear Thomson scattered x rays [7]. They imaged the transverse intensity profile of the x-ray beam scattered from the electrons using a CCD camera and measured the x-ray yield using a silicon diode. A $10 \mu\text{m}$ thick Ag foil was placed in front of the detector to cut off low-energy x rays in order to obtain the nonlinear component of the Thomson scattering [7]. Figure 1.5 shows the azimuthal distribution of the intensity for the second harmonic where the crosses and triangles represent measurements of orthogonal laser polarization directions and the lines represent the theoretical prediction. These measurements were from a linearly polarized laser. Their results also confirmed the analytical predictions for nonlinear Thomson scattering.

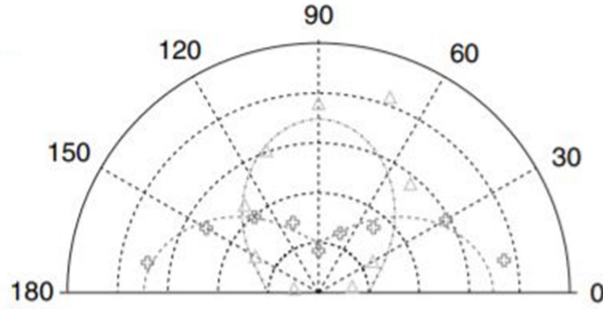


Figure 1.5 Azimuthal distribution of second harmonic from nonlinear Thomson scattered x rays from a linearly polarized laser, where the crosses and triangle represent measurements of orthogonal laser polarization directions and the lines represent the theoretical prediction. Figure taken from [7].

1.4 Quantum vs. Classical Electron

When considering radiation from individual electrons, we must consider the influence of the electron wave packet on the radiation. Our research group investigated the possibility of different portions of the electron wave packet interfering with each other and thus suppressing the radiation. If the electron is treated semiclassically, a vector potential is obtained with a classical current density as [8]

$$\mathbf{A}(\mathbf{r}, t) = \frac{\mu_0}{4\pi} \int d^3 r' \mathbf{J}(\mathbf{r}', t_r) / R, \quad (1.4)$$

where $R = |\mathbf{r} - \mathbf{r}'|$ and $t_r = t - R/c$. If we associate the quantum probability current with the classical current density \mathbf{J} , it has been shown that there is significant destructive interference in the scattered radiation \mathbf{A} in the perpendicular direction, especially when the electron wave-packet spreads to the size of the driving laser wavelength [9–11].

Our research group studied photoemission by a single-electron wave packet in a laser field using both relativistic semi-classical and quantum electrodynamic (QED) frameworks. Their results show that the amount of radiation is not influenced by the size of the electron wave packet, and single

electrons radiate with the strength of point emitters [11, 12].

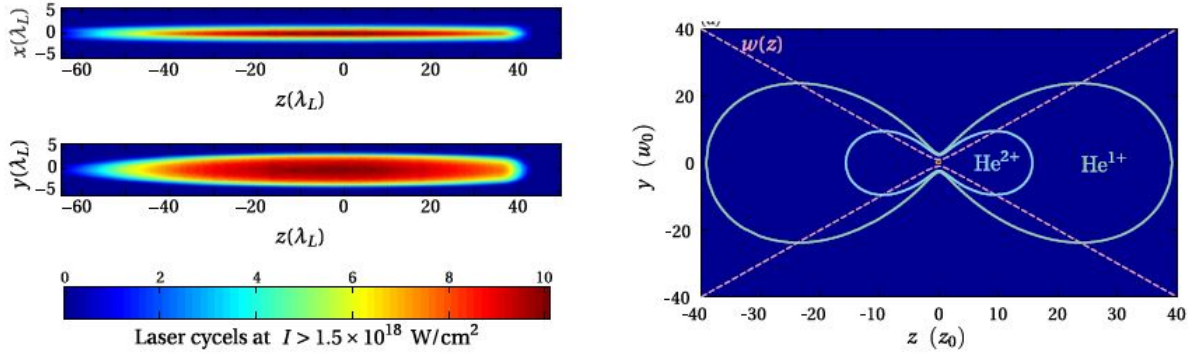


Figure 1.6 (Left) Two-dimensional images showing the $x - z$ plane and the $y - z$ plane where the electron experiences intensities around 10^{18} W/cm². (Right) Cross-section of laser focus showing the regions where first and second ionization of helium occurs. Figure taken from [13].

This theoretical prediction was confirmed experimentally by our research group as well. In their experiment, free electrons in very low density pressures (around 10^{-6} Torr) interact with a high-intensity laser field. Simulations showed that 10^{18} W/cm² was an ideal intensity, and as can be seen in Fig. 1.6, the region in which the electrons experience this high-intensity is very small compared to the region in which helium is ionized [13]. A weaker prepulse (2 mJ) was used to pre-ionize the helium and give the electron wave packets time to expand larger than the laser wavelength. The primary laser pulse (20 mJ) accelerates the electron wave packets causing the electrons to scatter light [14].

The experimental setup is shown in Fig. 1.7. At this high-intensity, the free electrons drift along the direction of the laser propagation at a significant fraction of the speed of light causing the scattered light to be red-shifted from the side-view [14]. The redshifted scattered light from the electrons peak around 900 nm [13] which allows for discrimination against the 800 nm laser wavelength. As shown in Fig. 1.7, the light scattered off of the electron wave packet is collected and focuses onto an optic fiber which sends the light to spectral filters. The spectral filters detect

light in the 875-925 nm range. The light is then sent to an avalanche photodiode (APD) for photon counting.

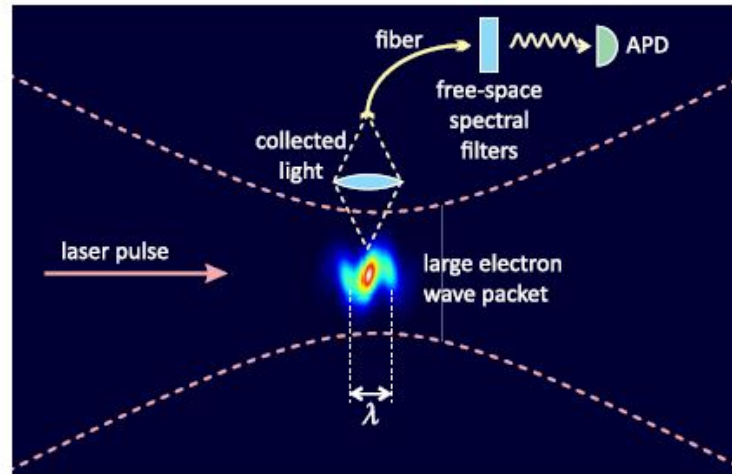


Figure 1.7 Experimental setup for previous research conducted by our research group. Scattered light from electron wave packet focused onto an optic fiber and sent through spectral filters to an APD. Figure taken from [14].

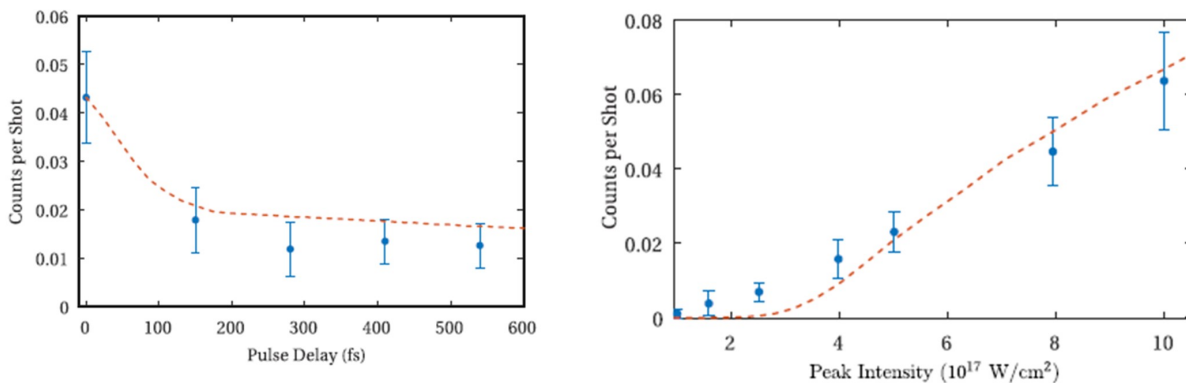


Figure 1.8 (Left) Number of photon counts per shot as a function of prepulse delay at a pressure of 10^{-5} Torr. (Right) Number of photon counts per shot as a function of laser intensity at a pressure of 3×10^{-5} Torr. The dashed lines show the computational models and the dots show experimental measurements with error bars giving the standard deviation. Figure taken from [14].

In order to see if the scattered radiation depends on the size of the electron wave packet, the

number of photon counts were taken for various prepulse delays, as shown on the left in Fig. 1.8. The factor of 2 drop in the signal was expected and accounts for two ionized electrons from helium atoms to drift apart enough so that they do not enhance each other's radiation [14]. If the size of the electron wave packet did influence the scattered radiation, we would expect to see a dramatically larger drop in the number of counts per shot for a large wave packet. Since the signal only shows the factor of 2 drop, the size of the electron wave packet does not influence the scattered radiation.

The number of photon counts per shot were also taken for various values of intensity with no prepulse, as shown on the right of Fig. 1.8. The dashed line shows the theoretical prediction from classical point emitters, and the dots show the experimental measurements. The data demonstrates that the electron wave packet radiates with the strength of classical point emitters. Therefore, it is appropriate to analyze our nonlinear Thomson-scattering experiments in a classical framework. These earlier experiments also pointed the way to look at nonlinear Thomson scattering using single-photon counting as a way of getting clean signal at very low densities where plasma effects could be minimized.

1.5 Overview

For my masters-thesis project, I have experimentally and theoretically studied nonlinear Thomson scattering from diffuse free electrons. We have used the techniques previously developed by our research group to measure polarization-resolved nonlinear Thomson scattering from free electrons. This technique allows us to distinguish individual photons scattered from electrons in the focus from the huge number of photons in the laser pulse. This technique is also done using pressures of around 1 Torr instead of atmospheric pressures used by the groups previously mentioned, and it gives very clean results. We have resolved the fundamental, second harmonic, and third harmonic of polarization-resolved nonlinear Thomson scattering from free electrons. Our results reasonably

match the theoretical prediction and show some asymmetry in the third harmonic. My research focused on setting up the experiment and positioning the detector on the high-intensity region in which nonlinear Thomson scattering occurs. I also measured the photon counts with respect to the detector angle.

Chapter 2 discusses the motion of the electron in a high-intensity laser beam and its radiation. Our experimental setup and methods is discussed. Chapter 4 presents our measurements for the first, second, and third harmonics. Our results show good agreement with theoretical predictions.

Chapter 2

Theoretical and Computational Model

2.1 Equations of Motion for an Electron in a High Intensity Laser Field

In 1970, Sarachik and Schappert analytically modeled the trajectory and radiation of an electron in a high-intensity electromagnetic plane wave [4]. They derived the equations that describe the motion of an electron moving relativistically as discussed in the previous chapter. Their report shows the trajectory in the electron's average rest frame, which is shown in Fig. 2.1. We review the equations that describe the trajectory of an electron in a high-intensity beam in this section.

As discussed in Chapter 1, the equations of motion for an electron moving in a high-intensity laser field are given by Eq. (1.1). As can be seen in this equation, the trajectory of the electron is affected by the electric and magnetic vector fields in the focal region. We model the vector fields using the analytic model developed by Erikson and Singh in 1994 for vector fields in the focal region [15]. Our research group has shown that the Singh model accurately approximates the field produced by a Gaussian beam reflected from a parabolic mirror. The relatively simple model represents the vector fields of the laser in the focal region [16]. According to the model, the electric

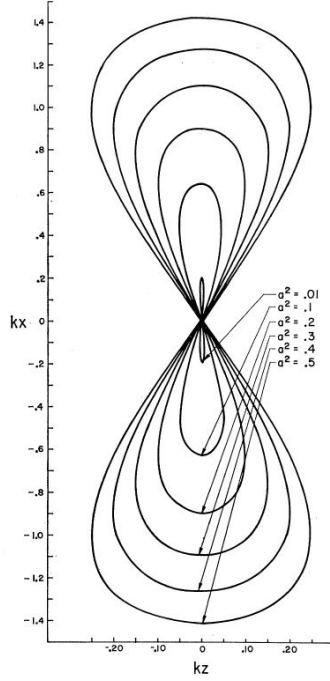


Figure 2.1 The electron trajectory in the electron's rest frame for various values of intensity in the $x - z$ plane. Figure taken from [4].

and magnetic fields are:

$$\mathbf{E}(x, y, z, t) = \text{Re} \left\{ E_p \left(\hat{x} + \frac{xy}{2\mathbb{Z}^2} \hat{y} - i \frac{x}{\mathbb{Z}} \hat{z} \right) \psi e^{i(kz - \omega t)} \boldsymbol{\varepsilon} \right\} \quad (2.1)$$

$$\mathbf{B}(x, y, z, t) = \text{Re} \left\{ \frac{E_p}{c} \left(\frac{xy}{2\mathbb{Z}^2} \hat{x} + \hat{y} - i \frac{y}{\mathbb{Z}} \hat{z} \right) \psi e^{i(kz - \omega t)} \boldsymbol{\varepsilon} \right\}, \quad (2.2)$$

where $\mathbb{Z} = z_0 + iz$, $\psi = \frac{z_0}{\mathbb{Z}} e^{-\frac{k\rho^2}{2\mathbb{Z}}}$, and $\rho^2 = x^2 + y^2$. Our envelope function is given by $\boldsymbol{\varepsilon} = e^{-\frac{\left(t - \frac{z + \rho^2/2R}{c}\right)^2}{\tau^2}}$, where $R = z + \frac{z_0^2}{z}$ and z_0 is the Rayleigh range.

We can make these equations dimensionless by letting $r' = kr$, $t' = \omega t$, $u' = u/c$, $\mathbf{p}' = \mathbf{p}/mc$, and $E' = \frac{E}{kmc^2/q}$. Then our equations of motion for the electron become:

$$\frac{d\mathbf{p}'}{dt'} = \mathbf{E}' + \mathbf{u}' \times \mathbf{B}' \quad (2.3)$$

$$\mathbf{p}' = \gamma \mathbf{u}' \quad (2.4)$$

$$\gamma = \frac{1}{\sqrt{1 - u'^2}}, \quad (2.5)$$

and our electric and magnetic fields are given by:

$$\mathbf{E}'(x', y', z', t') = \text{Re} \left\{ E_p' \left(\hat{x} + \frac{x'y'}{2\mathbb{Z}'^2} \hat{y} - i \frac{x'}{\mathbb{Z}'} \hat{z} \right) \psi e^{i(z'-t')} \boldsymbol{\varepsilon} \right\} \quad (2.6)$$

$$\mathbf{B}'(x', y', z', t') = \text{Re} \left\{ \frac{E_p'}{c} \left(\frac{x'y'}{2\mathbb{Z}'^2} \hat{x} + \hat{y} - i \frac{y'}{\mathbb{Z}'} \hat{z} \right) \psi e^{i(z'-t')} \boldsymbol{\varepsilon} \right\}, \quad (2.7)$$

where $\mathbb{Z}' = z'_0 + iz'$ and $z'_0 = kz_0$, $\psi = \frac{z'_0}{\mathbb{Z}'} e^{-\frac{\rho'^2}{2\mathbb{Z}'}}$, and $\rho'^2 = x'^2 + y'^2$. Our envelope function is now given by $\boldsymbol{\varepsilon} = e^{-\frac{(t'-z'+\rho'^2/2R')^2}{\tau'^2}}$, where $R' = z' + \frac{z'_0^2}{z'}$.

It is convenient for us to write \mathbf{u}' and γ in terms of p' . With some algebra, it can be shown that $\gamma = \sqrt{1 + p'^2}$. Then our differential equation is

$$\frac{d\mathbf{p}'}{dt'} = \mathbf{E}' + \frac{\mathbf{p}'}{\gamma} \times \mathbf{B}'. \quad (2.8)$$

It can also be shown that the acceleration of the electron is given by:

$$\mathbf{a}' = \frac{d\mathbf{u}'}{dt'} = \frac{1}{\gamma} [\mathbf{E}' + \mathbf{u}' \times \mathbf{B}' - \mathbf{u}'(\mathbf{u}' \cdot \mathbf{E}')]. \quad (2.9)$$

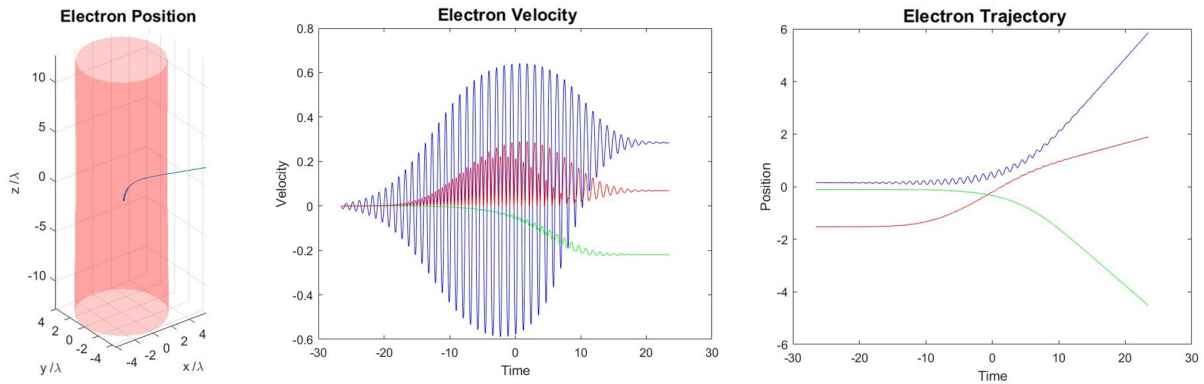


Figure 2.2 The position (left), velocity (center), and trajectory (right) of an electron that is initially slightly out of the focus of a high-intensity (1.5×10^{18} W/cm²) laser beam. The red cylinder in the left frame represents the laser beam and the blue line represents the electron position with respect to time. The blue, red, and green lines in the next two frames represent the x , y , and z components of the velocity and trajectory respectively.

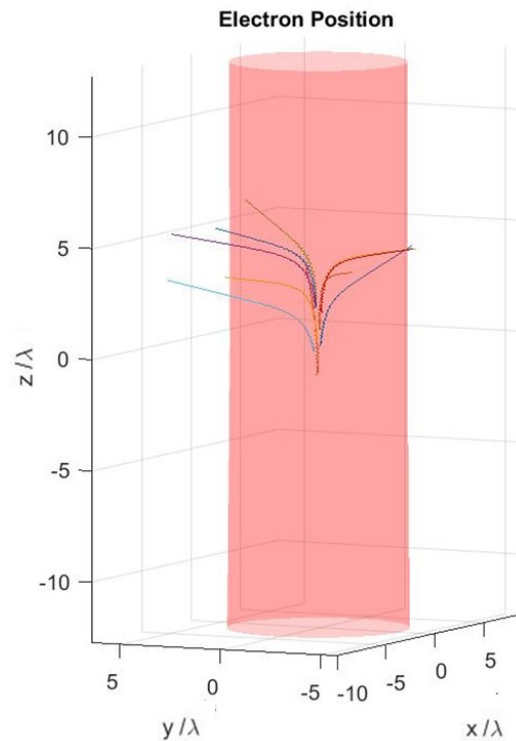


Figure 2.3 Trajectories of ten electrons with random initial positions in the focal region. Each line of a different color represents the position of one electron with respect to time, and the red cylinder represents the laser beam.

The solution to the differential equation given by the Lorentz force law will allow us to find the position (originating from the focal center), velocity, and acceleration of the electron. This differential equation must be solved numerically using a computer program. We have used the ode45 differential equation solver in Matlab to solve the equation and determine the electron's position, velocity, and acceleration. The first frame in Fig. 2.2 shows the electron's position in the lab frame where the red cylinder represents our laser beam and the blue line represents the electron position with respect to time. The next two frames show the electron's velocity and trajectory as a function of time. The blue, green, and red lines represent the x , y , and z components respectively.

Figure 2.3 shows the trajectory of ten electrons with random initial positions in the focal region.

There is also a random phase applied to the laser field because experimentally the phase of the laser will vary from shot to shot. We can see from Fig. 2.3 that the electrons get shot quickly out of our laser beam, but while the electrons are being accelerated in the focal region, they scatter light. The equations that govern this radiation are discussed in the following section.

2.2 Radiation from Free Electrons

Now that we have found expressions for the velocity and acceleration of electrons in a high-intensity laser field, we can use them to determine the electric and magnetic fields radiated by the electrons. The electric and magnetic fields for a moving point charge are found using the Liénard-Wiechert potentials [8] and can be approximated as:

$$\mathbf{E}_S(\mathbf{r}_d, t_d) = \frac{qk}{4\pi\epsilon_0 r_d} \frac{1}{(1 - \hat{\mathbf{r}}_d \cdot \mathbf{u}/c)^3} \hat{\mathbf{r}}_d \times \left((\hat{\mathbf{r}}_d - \mathbf{u}/c) \times \frac{\mathbf{a}}{c^2 k} \right) = \frac{qk}{4\pi\epsilon_0 r_d} \frac{\hat{\mathbf{r}}_d \times ((\hat{\mathbf{r}}_d - \mathbf{u}') \times \mathbf{a}')}{(1 - \hat{\mathbf{r}}_d \cdot \mathbf{u}')^3} \quad (2.10)$$

$$\mathbf{B}_S(\mathbf{r}_d, t_d) = \hat{\mathbf{r}}_d \times \frac{\mathbf{E}_S(\mathbf{r}_d, t_d)}{c}, \quad (2.11)$$

where \mathbf{r}_d is the detector position and t_d is the time at the detector when the field is measured. We can define $\mathbf{L} = \frac{\hat{\mathbf{r}}_d \times ((\hat{\mathbf{r}}_d - \mathbf{u}') \times \mathbf{a}')}{(1 - \hat{\mathbf{r}}_d \cdot \mathbf{u}')^3}$ to simplify our expression. The Poynting vector indicates the direction of flow of intensity and is given by:

$$\mathbf{S}(\mathbf{r}_d, t'_d) = \epsilon_0 c \left[\frac{qk}{4\pi\epsilon_0 r_d} \right]^2 L^2(\mathbf{r}_d, t'_d), \quad (2.12)$$

where the dimensionless detector time is $t'_d = t' + \mathbf{r}_d/c - \hat{\mathbf{r}}_d \cdot \mathbf{r}'$.

Since we are resolving longitudinal and azimuthal polarization, we must split \mathbf{L} up into longitudinal and azimuthal components. Using spherical coordinates, we obtain $\mathbf{L} = \hat{\mathbf{r}}_d L_{r_d} + \hat{\boldsymbol{\theta}} L_{\theta} + \hat{\boldsymbol{\phi}} L_{\phi}$, where $L_{r_d} = \hat{\mathbf{r}}_d \cdot \mathbf{L} = 0$, $L_{\theta} = \hat{\boldsymbol{\theta}} \cdot \mathbf{L}$, and $L_{\phi} = \hat{\boldsymbol{\phi}} \cdot \mathbf{L}$. This gives $L_{\theta} = L_x \cos \theta \cos \phi + L_y \cos \theta \sin \phi - L_z \sin \theta$ and $L_{\phi} = -L_x \sin \phi + L_y \cos \phi$. The intensity along these components is thus:

$$S_{\theta}(\mathbf{r}_d, t'_d) = \epsilon_0 c \left[\frac{qk}{4\pi\epsilon_0 r_d} \right]^2 L_{\theta}^2 \quad (2.13)$$

$$S_{\phi}(\mathbf{r}_d, t'_d) = \epsilon_0 c \left[\frac{qk}{4\pi\epsilon_0 r_d} \right]^2 L_{\phi}^2. \quad (2.14)$$

We are interested in the energy per steradian, or angular fluence so that we can determine the number of photons scattered. Integrating the intensity with respect to area will give us the power scattered by the electron, which we can write as:

$$P = \int_0^{2\pi} d\phi \int_0^{\pi} d\theta \sin\theta P_{\Omega}, \quad (2.15)$$

where $P_{\Omega} = r_d^2 S(\mathbf{r}_d, t'_d)$ is the power per steradian. Our collection system collects from a 7/8" diameter aperture that is 2" from the focus, which gives a solid angle of 0.15 steradian. Since this is a small solid angle, we can approximate the power as $P = 0.15P_{\Omega}$.

Now to get the energy per steradian, we integrate over time:

$$\Phi_{\Omega} = \int_{-\infty}^{\infty} P_{\Omega} dt_d = \epsilon_0 c \left[\frac{qk}{4\pi\epsilon_0 r_d} \right]^2 \int_{-\infty}^{\infty} L^2 \frac{dt'_d}{\omega} = \frac{q^2}{8\pi\epsilon_0 \lambda} \int_{-\infty}^{\infty} L^2 dt'_d. \quad (2.16)$$

This can be evaluated for both L_{θ}^2 and L_{ϕ}^2 for the different polarization components, and we finally multiply by 0.15 steradians to get the energy that reaches our detector.

Our experiment also requires separating the field into harmonic components. We do this by taking the Fourier transforms of L_{θ} and L_{ϕ} :

$$L_{\theta}(f) = \frac{1}{\sqrt{2\pi}} \int_{-\infty}^{\infty} L_{\theta}(t') e^{-i2\pi f t'} dt' \quad (2.17)$$

$$L_{\phi}(f) = \frac{1}{\sqrt{2\pi}} \int_{-\infty}^{\infty} L_{\phi}(t') e^{-i2\pi f t'} dt', \quad (2.18)$$

where f is a dimensionless frequency in which $f = 1$ corresponds to the fundamental frequency, and $f = N$ corresponds to the N^{th} harmonic. Parseval's theorem tells us that $\int_{-\infty}^{\infty} L^2(t'_d) dt'_d \propto \int_{-\infty}^{\infty} L^2(f) df$. Thus the amount of energy within a narrow band f_1 to f_2 that reaches the detector is:

$$\epsilon = (0.15) \left(\frac{q^2}{8\pi\epsilon_0 \lambda} \right) \left(\int_{-\infty}^{\infty} L^2 dt'_d \right) \frac{\int_{f_1}^{f_2} L^2(f) df}{\int_0^{\infty} L^2(f) df}. \quad (2.19)$$

Using a wavelength of $\lambda = 800$ nm, the laser photon energy is $\frac{hc}{\lambda} = 1.55$ eV. The number of photons in the band is then:

$$N = \frac{\epsilon}{f \cdot 1.55 \text{ eV}}, \quad (2.20)$$

where f represents the frequency in the narrow band from f_1 to f_2 .

To simulate our experiment, we will find the radiation patterns averaged over many initial electron positions in the focal region. A visualization of the averaged radiation from 500 electrons in the focal region of a laser beam is shown in Fig. 2.4. The vertical cones in the images represent the laser beam with its focus at the origin, and the radiation pattern is the far field radiation from an electron in the focus. The colors from dark to light represent increasing intensity. As mentioned previously, the electrons in a high-intensity laser field radiate harmonic frequencies of the incident light. The longitudinal and azimuthal components of the fundamental signal, second, and third harmonics radiated are shown in Fig. 2.4.

Taking a slice along the equator of these radiation patterns, we obtain a plot of the intensity as a function of angle. The first image on Fig. 2.5 shows the plane that these patterns are in, which is perpendicular to the laser propagation. The longitudinal and azimuthal components of the polarization are shown in red and blue respectively. From Fig. 2.5, we can see that the magnitude of the intensity decreases as the harmonic order increases.

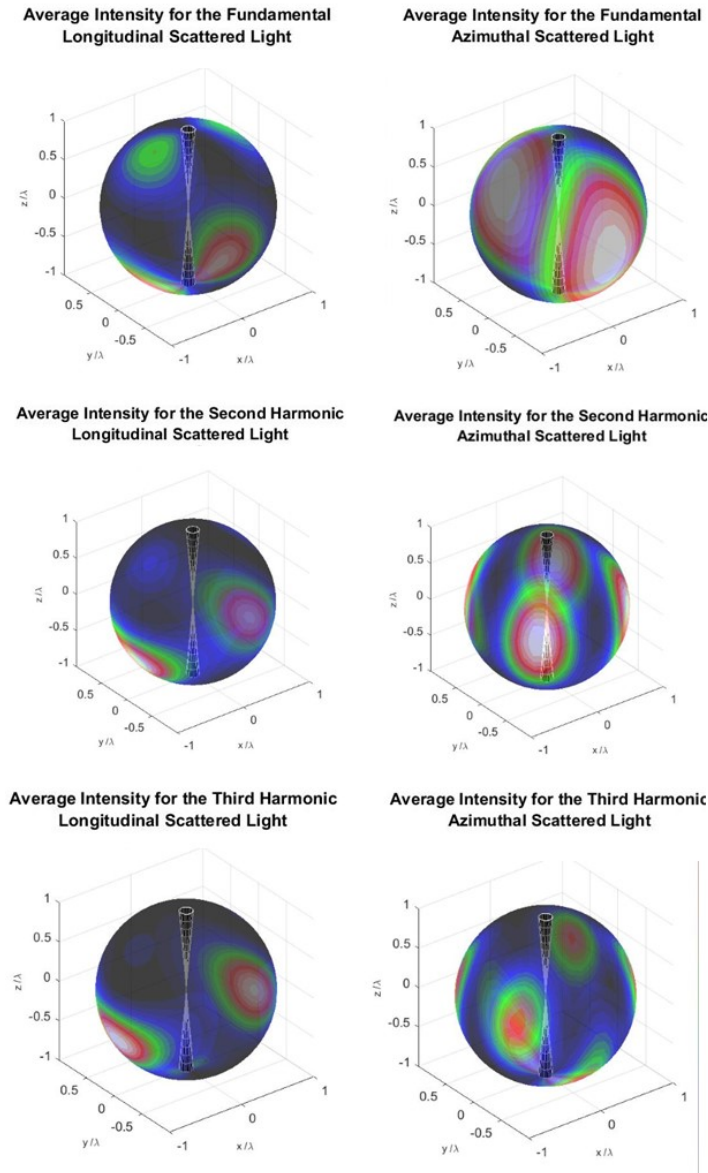


Figure 2.4 Average far-field radiation patterns of 500 electrons initially at the center of the sphere in a $1.5 \times 10^{18} \text{ W/cm}^2$ laser pulse with a fundamental wavelength of 800 nm. The black cones represent the laser focus and the colors represent different values of intensity where white is high intensity and black is low intensity. The longitudinal and azimuthal polarization components of the fundamental, second, and third harmonic are shown.

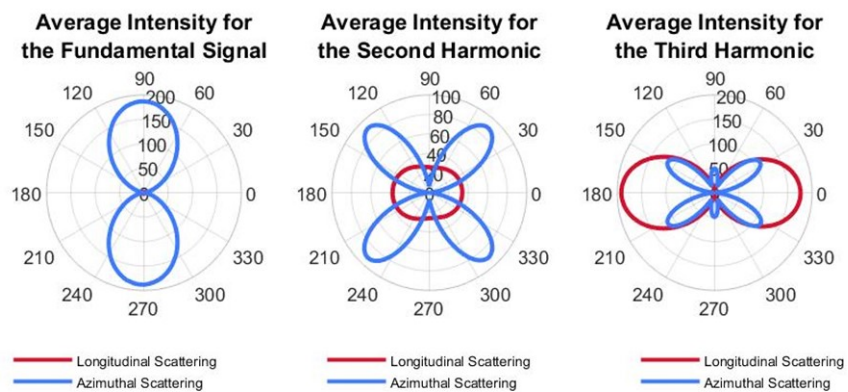


Figure 2.5 Far-field radiation patterns as a function of angle averaged over 500 electrons in a $1.5 \times 10^{18} \text{ W/cm}^2$ laser pulse with a fundamental wavelength of 800 nm. The blue and red lines represent the theoretical prediction for the azimuthal and longitudinal components respectively. The average intensity for the fundamental signal, the second harmonic, and the third harmonic are shown.

Chapter 3

Methods

3.1 Experimental Setup

Our experimental setup for measuring nonlinear Thomson scattering is very similar to the setup discussed in Section 1.4. We use a Ti:sapphire laser system that produces 50 mJ pulses of 800 nm light with a pulse duration of 38 fs, which we measured using a frequency-resolved optical grating (FROG). The pulse laser beam focuses using a parabolic mirror so that in the focal region we achieve intensities above 10^{18} W/cm². We use a high-resolution (3.45×3.45 μm) camera to measure the spot while we adjust pointing. We eliminate astigmatism and optimize the focus to achieve the smallest possible focal spot, which is around 5 μm in diameter.

As can be seen in the left image of Fig. 3.1, the laser beam (shown in red) enters our vacuum chamber and is focused by the parabolic mirror. The vacuum chamber is evacuated and filled with low-density helium (less than 1 Torr). The helium atoms in the laser field ionize, and the free electrons in the high-intensity focal region scatter radiation. The light that the electrons scatter is redshifted so that the fundamental 800 nm light has an emission peak around 900 nm. The second and third harmonics are redshifted from 400 nm to 450 nm and 266 nm to 300 nm respectively.

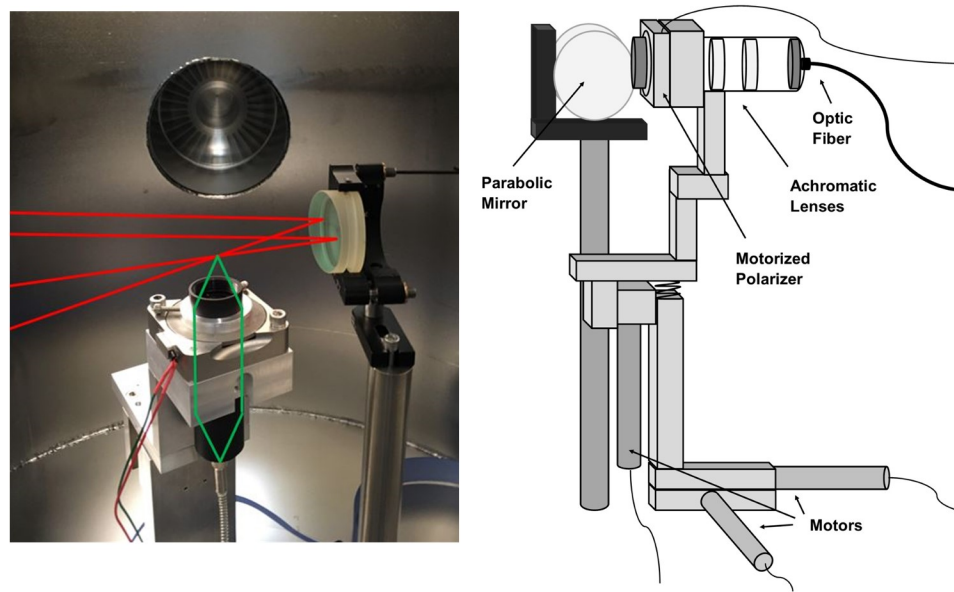


Figure 3.1 Left: (Side view) Laser light being focused by a parabolic mirror; light emitted from the focus being collected by the detector. Right: (Front view) Schematic of experimental setup.

Scattered light (shown in green in Fig. 3.1) goes through a motorized polarizer which allows us to switch between the longitudinal and azimuthal components of the polarization. A pair of achromatic lenses focus it into the optic fiber cable. Different sets of achromatic lenses associated to the wavelengths of the fundamental signal and the second and third harmonics are used to measure each harmonic. Having the optic fiber cable at the bottom of the tube containing the achromatic lenses helps to block out other light scattering around the vacuum chamber. A waveplate, not shown in the image, is also located upstream of the laser so that we can change the detection angle by rotating the linear polarization of the laser instead of having to rotate the detector around the focus.

The schematic shown in Fig. 3.1 has the parts of our setup labeled and shows the detector at

a 90 degree angle. We determined that having the detector at 90 degrees provided the cleanest measurements. The schematic also shows the vertical and horizontal motors that allow us to center our detector on the focus. Since our focus is only about 5 μm in diameter, aligning the collection system requires care.

The light collected by the optic fiber cable is sent through bandpass filters to isolate wavelengths associated to each harmonic. For the fundamental signal two 850 nm longpass cutoffs and one 900 nm bandpass filter with a 40 nm width are used. For the second and third harmonics, a 450 nm bandpass filter with a 10 nm width and a 310 nm bandpass filter with a 10 nm width are used respectively. As mentioned previously, since the scattered radiation is redshifted from the laser wavelength, the bandpass filters allow us to pass the signal from the scattered radiation and block the light coming from the laser pulse.

An avalanche photodiode (APD) is used to count photons for the fundamental signal and the second harmonic. A photomultiplier tube (PMT) is used for the third harmonic. The signal is time stamped relative to the arrival of the laser pulse. This setup allows us to distinguish individual photons coming from the nonlinear Thomson scattering from the millions of other photons being scattered.

3.2 Positioning the Detector

As mentioned previously, aligning the collection system requires care due to the small size of the focus. To add to the difficulty of this task, the position of the focus changes slightly as the vacuum chamber is evacuated of air and taken down to low pressures. We found a viable method of positioning the detector on the focal region.

We begin by sending diode laser light with the same frequency as the harmonic we are looking for into the vacuum chamber through the optic fiber cable shown in Fig. 3.1. This back-propagating

light is focused by the achromatic lenses and focuses at the location where the lens system will collect light a couple of centimeters above the motorized polarizer. We align the pointing mirrors on our high-intensity laser so that the high-intensity focus occurs at the collection focus. Once they are aligned, we connect the optic fiber cable to a spectrometer to see the emission spectrum of the radiation at atmospheric pressure. We choose a peak in the emission spectrum that has a wavelength close to the harmonic we are measuring and use the vertical and horizontal motors to position the collection lenses until the emission peak is maximized. As we evacuate the vacuum chamber, we continue to adjust the collection position so that the emission peak is still maximized. This allows us to decrease the pressure without losing the position of the focus.

Once the pressure is low enough that the emission peaks are no longer visible with the spectrometer, we rely on photon counting from the electrons themselves to fine-tune the position of the focus. We discuss this fine-tuning in the next section.

3.3 Photon Counting

Using a Labview program created by our research group, we count the number of photons emitted over a given time interval. To find the position of our high-intensity region in the focus, we do spatial scans along the laser beam, the side-to-side dimension and the vertical dimension in which we plot the number of counts with respect to position. We search for the peaks in each of these dimensions and center on them. By rotating the waveplate and the motorized polarizer, we verify that the number of counts is dependent on polarization.

The photon counts from the nonlinear Thomson scattering occur in a very narrow time window (a few nanoseconds), as shown in Fig. 3.2. This figure shows histograms obtained for the fundamental signal, and the second and third harmonics. The histograms for the fundamental signal and second harmonic show a peak in counts at around 67 ns, and the histogram for the third harmonic shows a

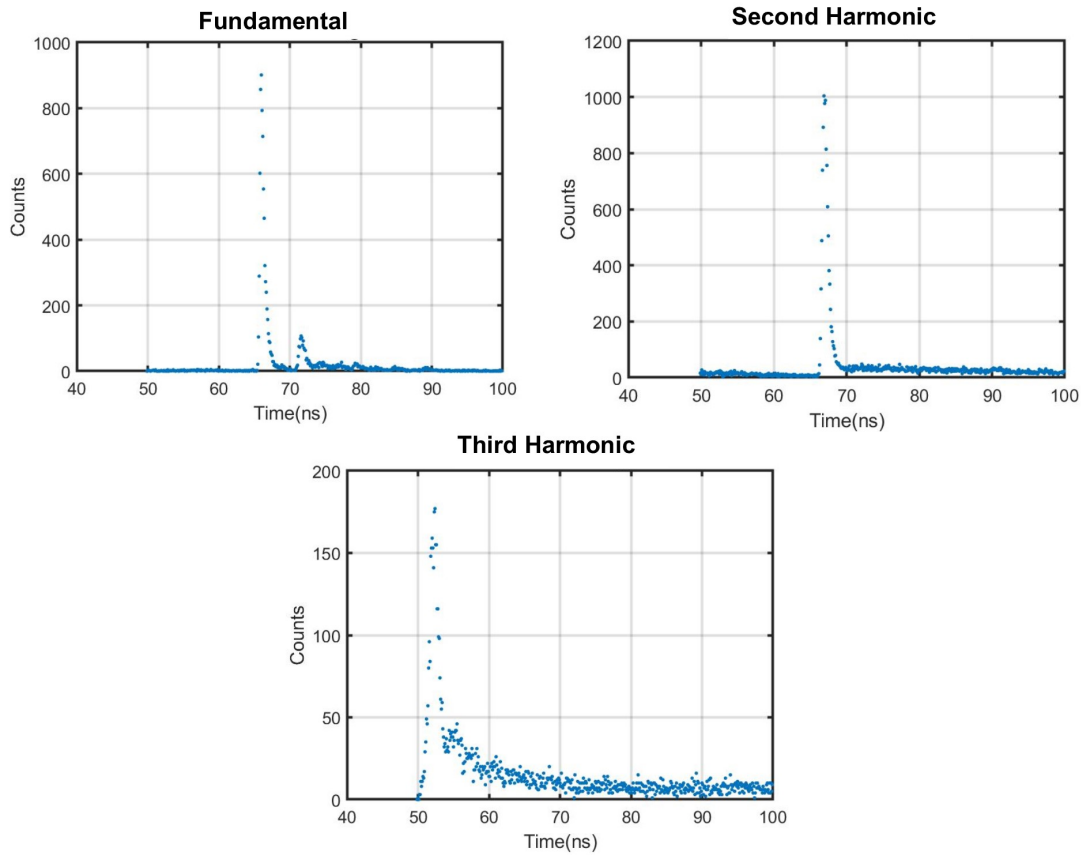


Figure 3.2 Fundamental signal, second harmonic, and third harmonic histograms are shown. Histograms show the total number of photon counts with respect to arrival time at the photon counter collected over thousands of laser shots during experimental measurements. The photons from the narrow peaks are the photons from nonlinear Thomson scattering.

peak in counts at around 53 ns. The position of the peak is different for the third harmonic because a PMT is used for third harmonic instead of the APD that is used for the fundamental signal and the second harmonic. The fact that these peaks occur in such narrow time windows is another indicator that the counts are from nonlinear Thomson scattering instead of from recombination light.

Once we determine that the collection lenses are positioned on the high-intensity region, we plot the number of counts from nonlinear Thomson scattering in a given time interval with respect to angle. We use a time interval of 100 seconds, or 1000 laser shots, and rotate the wave plate for

each data point to achieve these plots. We also rotate the motorized polarizer 90 degrees to switch between the longitudinal and azimuthal polarization components for each data point. We did this for the fundamental signal, and the second and third harmonics. Our results will be discussed in the following chapter.

Chapter 4

Results

4.1 Measurements of Nonlinear Thomson Scattering

The data achieved for the fundamental signal, the second harmonic, and the third harmonic were all taken with a laser energy of 25 mJ. The estimated intensity in the focal region was 1.5×10^{18} W/cm². An APD was used for the data taken for the fundamental signal and the second harmonic, and a PMT was used for the third harmonic. The number of photon counts in 100 seconds, or 1000 laser shots, were taken for each data point represented by dots in the figures discussed below.

4.1.1 Fundamental Radiation

The theoretical prediction and the data achieved for the fundamental signal are shown in the left and right images of Fig. 4.1. The ambient pressure was at 1.1×10^{-2} Torr. The emission pattern for the fundamental signal matches very closely to the theoretical result. As can be seen in Fig. 4.1, the photon counts go to zero as the detector angle goes to 0° and 180°. The fundamental signal only contains the azimuthal polarization component as the longitudinal polarization component goes to zero for the fundamental signal because the detector is perpendicular to the focus.

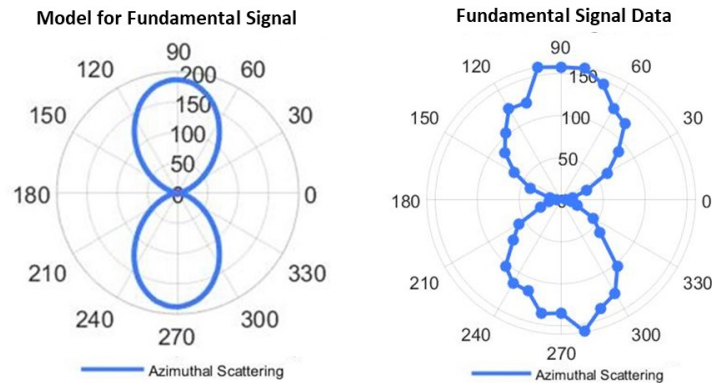


Figure 4.1 (Left) Theoretical prediction for fundamental radiation with respect to detector angle (Right) photon counts with respect to detector angle. Azimuthal scattering is shown in blue.

4.1.2 Second Harmonic

Figure 4.2 shows the theoretical prediction and the data for the second harmonic, which was taken at a pressure of 3.1×10^{-2} Torr. The emission pattern for the second harmonic signal matches closely to the theoretical result for the azimuthal and longitudinal polarizations. Our data shows that the peaks of the longitudinal component are smaller in magnitude than those of the azimuthal component.

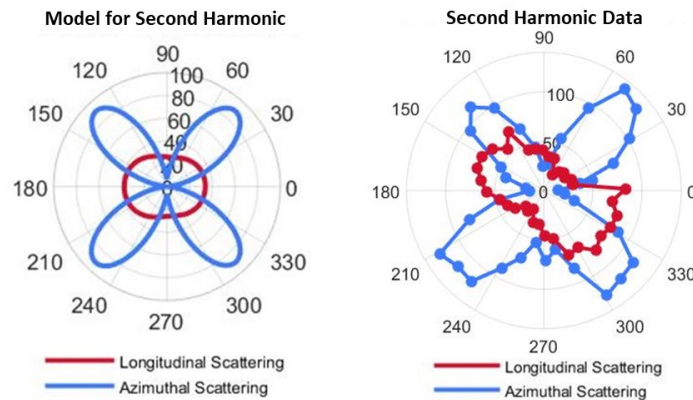


Figure 4.2 (Left) Theoretical prediction for second harmonic radiation with respect to detector angle (Right) photon counts with respect to detector angle. Azimuthal and longitudinal scattering are shown in blue and red respectively.

4.1.3 Third Harmonic

The theoretical prediction and the data for the third harmonic are shown in Fig. 4.3. A higher pressure of 1.45 Torr is required for measuring the third harmonic since the third harmonic signal is much weaker than the fundamental signal or the second harmonic. As shown in Fig. 4.3, the emission pattern for the third harmonic signal shows good agreement with the theoretical result. The longitudinal polarization is larger in magnitude than the azimuthal polarization, as expected from the theoretical result.

Our data also shows asymmetry in the petals for the azimuthal polarization, and we are investigating the cause for this asymmetry. Since the parabolic mirror used in the experiment is an off-axis parabolic mirror, further study on the vector fields from an off-axis parabolic mirror is required in order to know if the off-axis parabolic mirror is causing the asymmetry.

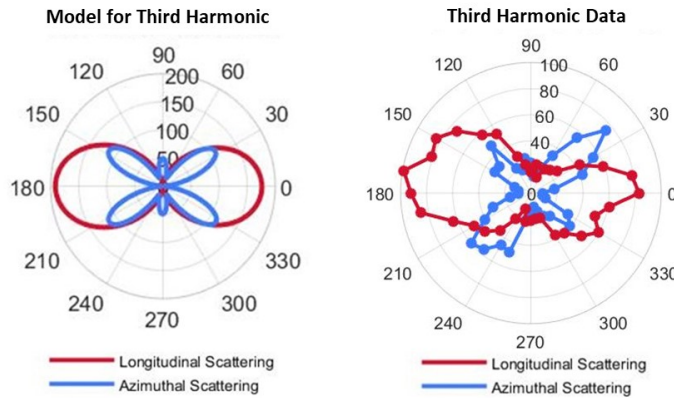


Figure 4.3 (Left) Theoretical prediction for third harmonic radiation with respect to detector angle (Right) photon counts with respect to detector angle. Azimuthal and longitudinal scattering are shown in blue and red respectively.

Since these measurements were taken at such low pressures, they are unaffected by plasma effects and thus give a clean visualization of nonlinear Thomson scattering. This is a significant advancement over past measurements which were made at atmospheric pressures. These results are the first polarization-resolved measurements of both the second harmonic and the third harmonic of

nonlinear Thomson scattering and confirm the theoretical prediction. The polarization components increase our understanding of Thomson scattering.

4.2 Summary

In conclusion, we have successfully measured the fundamental signal, the second harmonic and the third harmonic of polarization-resolved nonlinear Thomson scattering using a high-intensity laser and single-photon detectors. The method we have performed for measuring nonlinear Thomson scattering gives clean results. As shown in the previous section, our results reasonably match the theoretical emission patterns for the fundamental signal and the second and third harmonics. The results also show some asymmetry in the third harmonic petals, which need further investigation.

4.3 Future Work

Our research group is studying other factors that can influence the Thomson scattering from free electrons. One of these is how using different gas species will affect the radiation; our group has performed this study using neon and argon instead of helium. Another topic of interest is how the peak laser intensity influences the scattered radiation. We have used intensity filters to conduct this experiment.

We can also gain further insight by changing the shape of our focus. We would like to know if intentionally adding astigmatism or elongating the focus affects the scattered radiation. Changing the focal shape will be investigated in future studies.

Bibliography

- [1] Y. Y. Lau, “Nonlinear Thomson scattering: A tutorial,” *Phys. Plasmas* 10 (2003).
- [2] S. Chen, A. Maksimchuk, and D. Umstadter, “Experimental observation of relativistic nonlinear Thomson scattering,” *Nature* **396**, 653–655 (1998).
- [3] E. Esarey, “Nonlinear Thomson scattering of intense laser pulses from beams and plasmas,” *Phys. Rev. E* 48 (1993).
- [4] E. S. Sarachik and G. T. Schappert, “Classical Theory of the Scattering of Intense Laser Radiation by Free Electrons,” *Phys. Rev. D* **1**, 2738–2753 (1970).
- [5] W. Yu, “Strong frequency up-conversion by nonlinear Thomson scattering from relativistic electrons,” *Phys. Plasmas* 5 (1998).
- [6] K. Lee and Y. H. Cha, “Relativistic nonlinear Thomson scattering as attosecond x-ray source,” *Phys. Rev. E* 67 (2003).
- [7] M. Babzien, I. Ben-Zvi, K. Kusche, I. Pavlishin, I. Pogorelsky, D. Siddons, and V. Yakimenko, “Observation of the Second Harmonic in Thomson Scattering from Relativistic Electrons,” *Phys. Rev. Lett.* 96 (2006).
- [8] D. J. Griffiths, *Introduction to Electrodynamics* (Pearson, 1999).

-
- [9] P. Krekora, R. E. Wagner, Q. Su, and R. Grobe, “Retardation and Kinematic Relativistic Effects in Scattered Light,” *Laser Phys* 12 (2002).
- [10] E. Chowdhury, I. Ghebregziabiher, and B. Walker, “Larmor radiation from the ultra-intense field ionization of atoms,” *J. Phys. B* 38 (2005).
- [11] J. Peatross, C. Muller, K. Z. Hatsagortsyan, and C. H. Keitel, “Photoemission of a Single-Electron Wave Packet in a Strong Laser Field,” *Phys. Rev. Lett.* **100**, 153601–153605 (2008).
- [12] J. Corson, J. Peatross, C. Muller, and K. Hatsagortsyan, “Scattering of intense laser radiation by a single-electron wave packet,” *Phys. Rev. A* 84 (2011).
- [13] G. Tarbox, M. Ware, E. Cunningham, R. Sandberg, and J. Peatross, “Radiation from free electrons in a laser focus at $10^{18} \text{W}/\text{cm}^2$: modeling of photon yields and required focal conditions,” *J. Opt. Soc. Am. B* 32 (2016).
- [14] M. Ware, E. Cunningham, C. Coburn, and J. Peatross, “Measured photoemission from electron wave packets in a strong laser field,” *Opt. Lett.* **41**, 689–692 (2016).
- [15] W. L. Erikson and S. Singh, “Polarization properties of Maxwell-Gaussian laser beams,” *Phys. Rev. E* 49 (1994).
- [16] J. Peatross, M. Berrondo, D. Smith, and M. Ware, “Vector fields in a tight laser focus: comparison of models,” *Opt. Express* **25**, 13990–14007 (2017).

Index

Compton scattering, 1

electron trajectory, 4, 13, 14

electron wave packet, 7–10

harmonic, 3–6, 10, 17, 18, 21, 23, 25, 27–30

Lorentz Force Law, 1, 2, 12, 15

parabolic mirror, 21, 22, 29

photon count, 9–11, 24, 27–29

photon detector, 30

polarization, 10, 16, 17, 19, 22, 24, 28–30

Singh model, 12

Thomson scattering, 1, 3–5, 10, 23, 30

vector fields, 12, 29